Transylvanian Review

Vol XXVI, No. 30, 2018

Transylvanian Review
Centrul de Studii Transilvane| str. Mihail Kogalniceanu nr. 12-14, et.5, Cluj-Napoca
Email: transylvanianreview@gmail.com
Online Submission System: http://transylvanianreviewjournal.org/

Study of the Heat Ventilation in a Box Prototype with the k-ω Turbulence Model

Badis Bakri[1,*], Slah Driss[1], Ahmed Ketata[1], Zied Driss[1], Hani Benguesmia[2] and Fareh Hamrit[2]

[1] Laboratory of Electro-Mechanic Systems (LASEM), National School of Engineers of Sfax (ENIS), University of Sfax, Tunisia
[2] Faculty of Technologies, University of M'sila, Algeria

Abstract

The use of efficient systems in order to reduce the energy consumption presents in nowadays a great challenge. Indeed, the use of the renewable energy in the heat ventilation of building application becomes very crucial. In this work, we are interested on the study of the turbulent flow in a box prototype. In this prototype, a solar system is integrated to supply the whole inlet with a hot air. The numerical model is based on the resolution of the Navier-Stokes equations in conjunction with the standard k-ω turbulence model. These equations were solved by a finite volume discretization method using the commercial CFD code ANSYS Fluent 17.0. To accurate the numerical results, the meshing effect on the numerical results was studied to choose the optimal mesh with a minimum calculated time. The numerical results were compared using anterior results developed in our laboratory. The good agreements confirm the validity of the numerical method.

Keywords: CFD, box prototype, heat ventilation, turbulent flow, meshing effect.

[*] Corresponding author: Laboratory of Electro-Mechanic Systems (LASEM), National School of Engineers of Sfax (ENIS), University of Sfax, Tunisia.

Introduction

The energy use worldwide is increasing every year. In the last 40 years, the consumption has more than doubled. In fact, we can affirm today that the CFD technique is a useful tool, largely adopted by the indoor environment research community (Nilsen, 2016) for investigations dealing with ventilation efficiency (Mao, 2016), indoor air quality (Gilani, 2015) and thermal comfort (Nada, 2016, Ahmed, 2016). The housing and service sector is one of the largest energy users on the word market. In order to reduce the energy consumption, the use of efficient systems presents a great role (Wang, 2009, Varughese, 2016). In this context, Park *et al.* (2017) investigated the effect of the interaction between buoyancy and wind on windward SSV in an isolated building. Driss *et al.* (2016) developed a living room with a patio system located in the building center. This patio, with transparent roofing, can stock great heat energy in winter. By connecting this patio to the adjacent rooms, these solutions can improve the comfort conditions by modifying the microclimate of the building and by enhancing the airflow in it. In other work, Driss *et al.* (2015) proposed an outlining environment suitable building, to develop the natural ventilation and provide the thermal comfort requirements around the building and by enhancing the airflow. Rauf *et al.* (2015) investigated the relationship between the service life and the life cycle embodied energy of buildings. The embodied energy of a detached residential building was calculated for a building service life range of 1-150 years. Premrov *et al.* (2016) demonstrated possible avoidance of the latter energy related problem. The research is based on a case study of a one-storey timber-frame house, taking into account the climate data for three different European cities. Chan (2015) investigated an appropriate floor level of a residential building above which balconies should be incorporated. Different building configurations coupled with microclimate conditions produced varying flow field around building complex have been investigated for many research, extensively, through wind tunnel measurement. In buildings, the natural ventilation occurs when there is a pressure weight contrasts generated by wind or buoyancy forces that act on one or more openings in the building envelope (Martins, 2016). It is agreed that variables influencing inside thermal comfort can be assembled into two groups: human factors and environmental factors. These factors include air temperatures, air velocity, mean radiant temperature and relative humidity (Sedik *et al.*, 2013). Air temperature is the most regularly utilized parameter of thermal comfort (Yang *et al.*, 2016). In others applications, Zhou *et al.* (2014) employed CFD simulation to optimize natural ventilation for high-rise residential buildings by adjusting the building orientation, building spacing, window opening positions. Caciolo *et al.* (2014) demonstrated that the natural ventilation can contribute to the reduction of the air conditioning demand and to the improvement of thermal comfort in buildings. Bu *et al.* (2013) studied the performance of both wind tunnel experiments and numerical simulations on a scale model with the focus on wind-driven natural ventilation in an areaway-attached basement with a single sided opening. Awbi (1998) presented results for natural convection heat transfer coefficients of a heated wall, a heated floor and a heated ceiling which have been calculated using CFD. Lo *et al.* (2012) provided measurements of wind properties, façade pressures, airflow rates through small window openings, and tracer gas concentrations for a multi-zone test building. While studies have focused on the difficulty of predicting the total flow rate and measuring opening characteristics of cross ventilation. In a second paper, Lo *et al.* (3013) investigated the impacts on the distribution of indoor air. Pasut *et al.* (2012) investigated the performance of the two most commonly used turbulence models for simulating the naturally ventilated DSF and results validated against available experimental data. Zhang *et al.* (2007) evaluated the overall performance of eight prevalent and recently proposed models for simulating airflows in enclosed environments. Niu (2004) proposed using window vents as an alternative for natural ventilation in high-rise buildings. His analysis showed that window vents can provide constant air flow by self-regulating the opening degree in response to pressure differences. According to theses anterior studies, it is clear that the use of the renewable energy in the building application becomes very crucial. Also, there are few researches on the design method. The aim of this work is to develop CFD simulations to study the turbulent flow in a box prototype. In this prototype, a solar system is integrated to supply the whole inlet with a hot air. To accurate the numerical results, we are interested on the study of the meshing effect on the numerical results to choose the optimal mesh with a minimum calculated time. The numerical results are validated using anterior results developed in our laboratory.

Geometrical System

Fig 1 presents a box prototype with a height h= 0.22 m, a width w= 0.20 m and a length l= 0.30 m. In this system, two square holes, with a distance h_3= h_4=0.02 m, are placed in the same face. The first hole, placed at a distance h_1= 0.05m from the floor, is used to give the airflow from the outside of the box prototype.

The second hole, placed at a distance h_2= 0.18 m from the base, permits the evacuation of the air flow from the box prototype. In practice, the air flow comes from a solar air system or from a patio with transparent roofing. As presented by Driss *et al.* (2016), this patio can stock the heat energy in winter. By connecting this patio to the adjacent rooms, it is possible to create a circulation of the heat flow which can be distributed according to the building. However, in our experimental investigation, we have used an air heater to supply the box prototype.

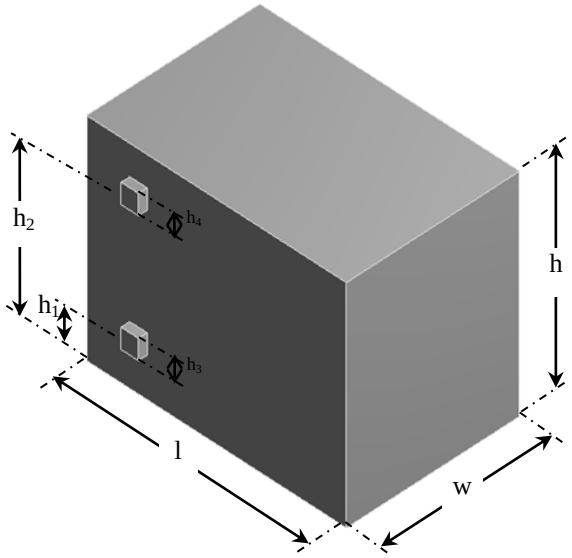

Fig 1: 3D View of the box prototype

Numerical Parameters

Mathematical Formulation

The equations governing the flow of air are the continuity equation, the momentum equations and the energy equation. Substituting expressions for the flow variables into the instantaneous continuity and momentum equations and taking a time average yields, the ensemble-averaged momentum equations can be obtained (Driss et *al.*, 2014, Driss et *al.*, 2015, Driss et *al.*, 2016). They can be written in Cartesian coordinate form as:

$$\frac{\partial p}{\partial t} + \frac{\partial}{\partial x_i}(pu_i) = 0 \quad (1)$$

$$\frac{\partial}{\partial t}(pu_i) + \frac{\partial}{\partial x_j}(pu_i u_j) = -\frac{\partial p}{\partial x_i} + \frac{\partial}{\partial x_j}\left[\mu\left(\frac{\partial u_i}{\partial x_j} + \frac{\partial u_j}{\partial x_i} - \frac{2}{3}\delta_{ij}\frac{\partial u_i}{\partial x_i}\right)\right] + \frac{\partial}{\partial x_j}\left(-p\,\overline{u'_i u'_j}\right) + F_i \quad (2)$$

These equations are called Reynolds-averaged Navier-Stokes (RANS) equations. They have the same general form as the instantaneous Navier-Stokes equations, with the velocities and other solution variables representing time-averaged values. Additional terms represent the effects of turbulence. These Reynolds stresses $-p\,\overline{u'_i u'_j}$ must be modeled in order to close equation 2. The Reynolds-averaged approach to turbulence modeling requires that the Reynolds stresses are appropriately modeled. A common method employs the Boussinesq hypothesis to relate the Reynolds stresses to the mean velocity gradients:

$$-\overline{pu_i u_j} = \mu_t\left(\frac{\partial u_i}{\partial x_j} + \frac{\partial u_i}{\partial x_i}\right) - \frac{2}{3}\left(pk + \mu_t\frac{\partial u_k}{\partial x_k}\right)\delta_{ij} \quad (3)$$

The Boussinesq hypothesis is used in the different turbulence models. The advantage of this approach is the relatively low computational cost associated with the computation of the turbulent viscosity μ_t, defined by:

$$\mu_t = \alpha^* \frac{pk}{\omega} \quad (4)$$

The coefficient α^*damps the turbulent viscosity causing a low-Reynolds number correction. It is given by:

$$\alpha^* = \alpha^*_\infty\left(\frac{\alpha^*_0 + Re_t/R_k}{1 + Re_t/R_k}\right) \quad (5)$$

Where:

$$Re_t = \frac{pk}{\mu\omega} \quad (6)$$

$$R_k = 6 \quad (7)$$

$$\alpha^*_0 = \frac{\beta_i}{3} \quad (8)$$

$$\beta_i = 0.072 \quad (9)$$

In the high-Reynolds number form of the k-ω model, $\alpha^*=\alpha^*_\infty = 1$. The standard k-ω model is based on the Wilcox k-ω model, which incorporates modifications for low-Reynolds number effects, compressibility, and shear flow spreading. With this model, the turbulence kinetic energy k and the specific dissipation rate ω are obtained from the following transport equations:

$$\frac{\partial}{\partial t}(pk) + \frac{\partial}{\partial x_i}(pku_i) = \frac{\partial}{\partial x_i}\left(\Gamma_\omega\frac{\partial k}{\partial x_j}\right) + G_k - Y_k + S_k \quad (10)$$

$$\frac{\partial}{\partial t}(p\omega) + \frac{\partial}{\partial x_i}(p\omega u_i) = \frac{\partial}{\partial x_j}\left(\Gamma_\omega\frac{\partial \omega}{\partial x_j}\right) + G_\omega - Y_\omega + S_\omega \quad (11)$$

Constants of the standard k-ω model are presented in table 1.

Table 1: Constants of the standard k-ω model.

α_0	α_∞	α^*_∞	R_ω	R_k	σ_k
1/9	1.9	1.0	2.95	6.0	2.0

The turbulent heat transport is modeled using the concept of the Reynolds analogy to turbulent momentum transfer. The "modeled" energy equation is as follows:

$$\frac{\partial}{\partial t}(pE) + \frac{\partial}{\partial x_i}[u_i(pE + p)] = \frac{\partial}{\partial x_j}\left[\left(k + \frac{c_p \mu_t}{Pr_t}\right)\frac{\partial T}{\partial x_j} + u_i(T_{ij})\right] + S_h \quad (12)$$

Where K is the thermal conductivity, E is the total energy, and $(\tau_{ij})_{eff}$ is the deviatoric stress tensor, defined as:

$$(\tau_{ij})_{eff} = \mu_{eff}\left(\frac{\partial u_j}{\partial x_i} + \frac{\partial u_i}{\partial x_j}\right) - \frac{2}{3}\mu_{eff}\frac{\partial u_k}{\partial x_k}\delta_{ij} \quad (13)$$

Boundary Conditions

A summary of the boundary conditions is given in Fig 2. In these conditions, we have considered that the heat flow supply the box prototype from the outside air heater with a velocity inlet equal to V= 3.4 m.s^{-1} and a temperature T= 310 K, measured in the first hole. From the second hole, the air flow is evacuated from the box prototype to an area with a static atmospheric pressure. For thus, we have imposed in the second hole an outlet pressure with a value of 101325 Pa. Knowing that the box prototype presents our domain, the roof and the lateral surface of the building and the wall of the computational domain are considered as a wall boundary conditions.

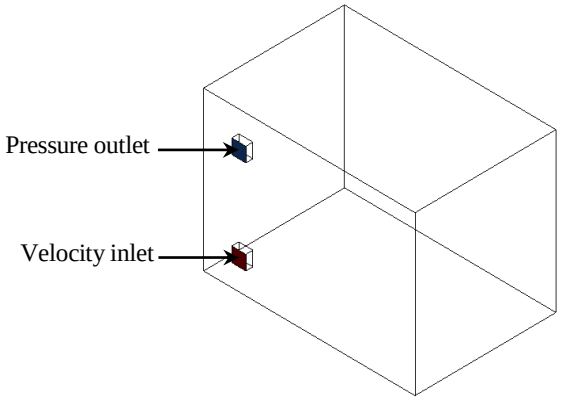

Fig 2: Boundary conditions

Meshing Choice and Experimental Validation

In this section, we are interested on the mesh resolution's influence on the velocity profile defined in the intersection of the two planes z= -0.005 m and x= 0.06 m. Particularly, we have superposed the experimental results, collected from the experimental investigation, with the numerical results for different meshing as presented in Fig 3. In fact, the type of the mesh has been changed based on the cells number. For thus, four meshes have been tested. The first case to be set corresponds to a coarse mesh composed by 12883 cells (Fig 3.a). The second case corresponds to 119061 cells (Fig 3.b) and the third case corresponds to 167400 cells (Fig 3.c). However, the fourth case corresponds to a refined mesh with 797416 cells (Fig 3.d). The corresponding time calculation and number of iterations for the different simulations are presented in tab 2. From these results, it has been observed that the velocity profiles seem to have the same appearance, but the velocity values depends on the meshing choice. In fact, more the size of the cells increases, the difference between the experimental and numerical results is great. In these conditions, it has been noted that the velocity value obtained with the third and the fourth cases are the closest to the experimental measured value. In these conditions, the gap between the numerical and the experimental results is about 5%. In addition, it was found that the time resolution increases with decreasing of the mesh size. For thus, our choice leads to a better result regarding the precision and resolution time. This study tends to show that the third meshing are the most efficient to model the air flow in the box prototype. (Fig 4)

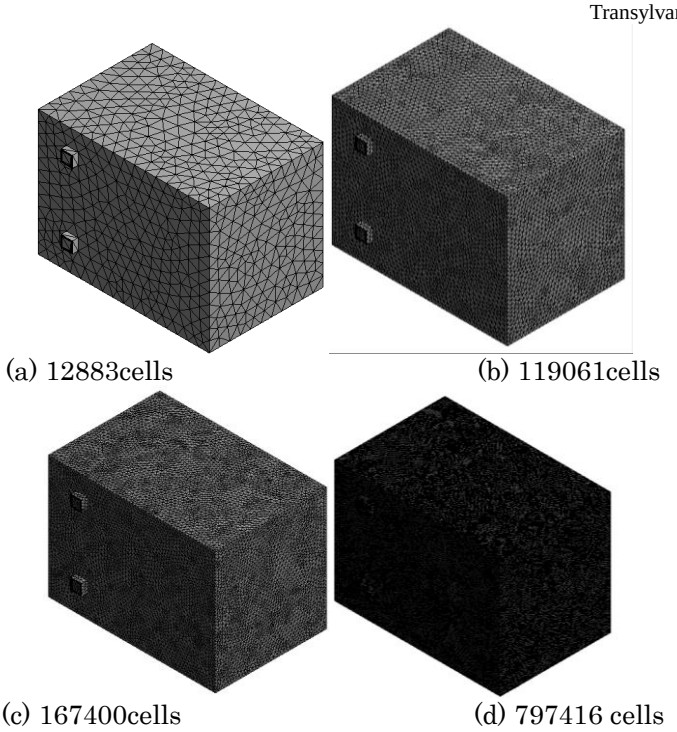

(a) 12883cells (b) 119061cells

(c) 167400cells (d) 797416 cells

Fig 3: Meshing of the computational domain

Table 2: Characteristic of the meshing

	Number of Nodes	Number of cells	Time calculation	Number of iterations
First Meshing	5004	12883	6:25:32	5738
Second Meshing	43825	119061	25:40:28	16668
Third Meshing	64312	167400	38:32:39	58154
Fourth Meshing	303189	797416	120:47:22	167208

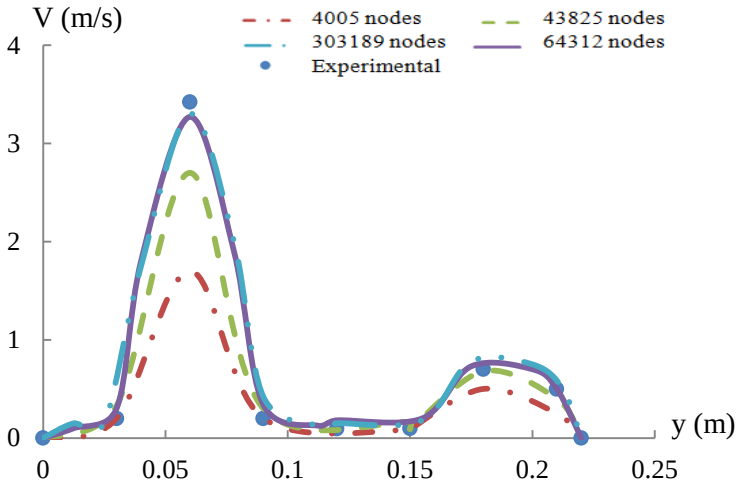

Fig 4: Velocity profiles in the direction defined by z= -0.005 m and x= 0.06 m.

Results and Discussion

In this section, we are interested in studying of the aerodynamic structure of the turbulent flow inside the box prototype, characterized by a Reynolds number equal to Re= 5100. Particularly, we have considered six planes, defined by x= 0.06 m, x= 0.20 m, y= 0.05 m, y= 0.18 m, z= -0.03 m and z= -0.14 m, to study the air flow characteristic such as the distribution of the velocity fields, the temperature, the total pressure, the turbulent kinetic energy and the turbulent viscosity, as presented in figure 5.

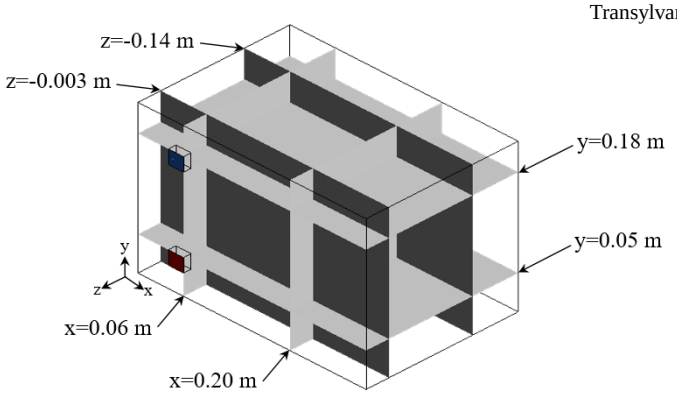

Fig 5: Visualization planes.

Velocity Fields

Fig 6 shows the distribution of the velocity fields in the different considered planes defined by x= 0.06 m, x= 0.20 m, y= 0.05 m, y= 0.18 m, z= -0.03 m and z= -0.14 m. According to these results, it has been noted that the average velocity is equal to V= 3.4 m s^{-1} at the entrance hole of the box prototype. From this hole, a discharge area has been generated until the opposite wall, where the averaged velocity value is about V= 1.3 m s^{-1}. In this crosswise, the direction of the velocity is modified in two directions. The first ascending flow generates the recirculation zone characterized by the center position defined by x= 0.06 m, y= 0.12 m and z= -0.13 m and appeared in the whole area of the box prototype. The second descending flow generates the dead zone characterized by the center position defined by x= 0.06 m, y= 0.02 m and z= -0.16 m and appeared in the down area. Through the hole outlet, the exiting movement of the air flow appears with a maximum value equal to V= 4.65 m s^{-1}. In this side, the averaged velocity presents a very low value.

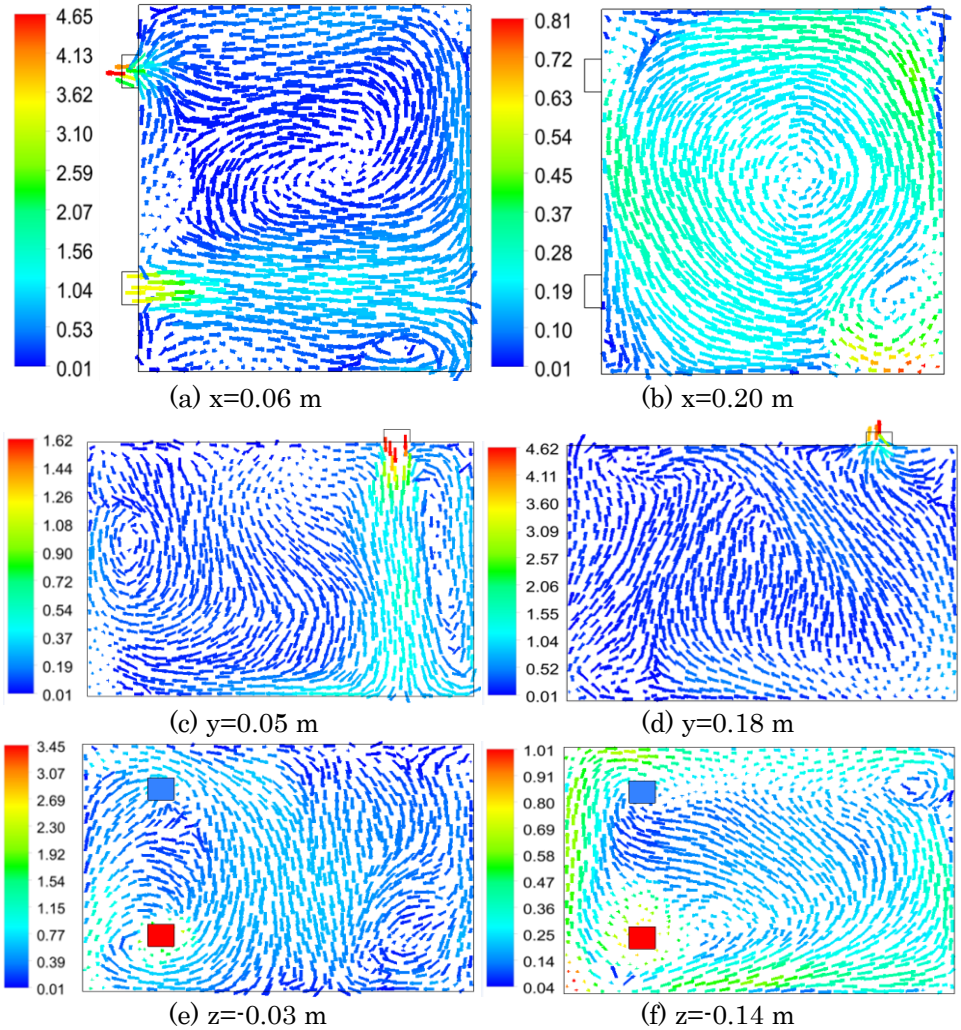

(a) x=0.06 m (b) x=0.20 m

(c) y=0.05 m (d) y=0.18 m

(e) z=-0.03 m (f) z=-0.14 m

Fig 6: Distribution of the velocity field.

Temperature

Fig 7 shows the distribution of the temperature at t= 2 s, in the different considered planes defined by x= 0.06 m, x= 0.20 m, y= 0.05 m, y= 0.18 m, z= -0.03 m and z= -0.14 m. According to these results, it has been noted that the temperature is equal to T= 310 K at the entrance hole of the box prototype. From this hole, a slightly decrease of the temperature has been observed in the discharge area developed until the opposite wall. Above this area, the temperature decreases further. This fact can be explained by the recirculation zone appeared in the whole area of the box prototype. This cooling continues until the hole outlet, where the temperature achieves T= 300 K. The cold area characteristics of the minimum value equal to T= 295 K appears in the dead zone localized between the two holes.

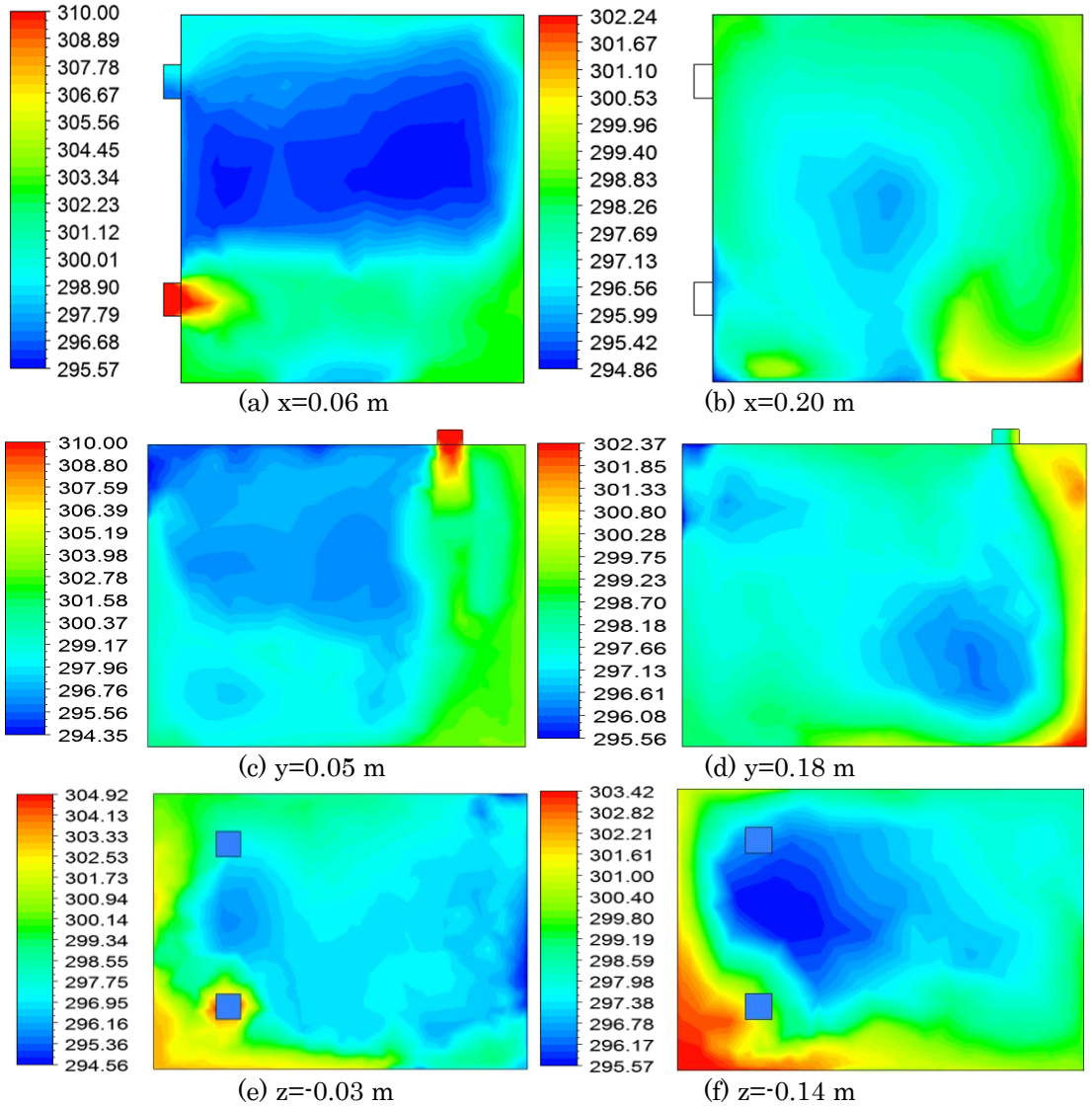

Fig 7: Distribution of the temperature at t=2 s.

Total Pressure

Fig 8 shows the distribution of the total pressure in the different considered planes defined by x= 0.06 m, x= 0.20 m, y= 0.05 m, y= 0.18 m, z= -0.03 m and z= -0.14 m. According to these results, it has been observed that the total pressure presents a compression zone at the entrance hole of the box prototype. From this hole, a slightly decrease of the total pressure has been noted in the discharge area. Indeed, a second compression zone characteristic of the maximum value of the total pressure, equal to p_t= 101342 Pa, is created in the opposite wall. This fact can be explained by the recirculation zone appeared in the whole area of the box prototype. In the hole outlet, a depression zone, characteristic of the minimum value of the total pressure equal to p_t= 101322 Pa, is shaped.

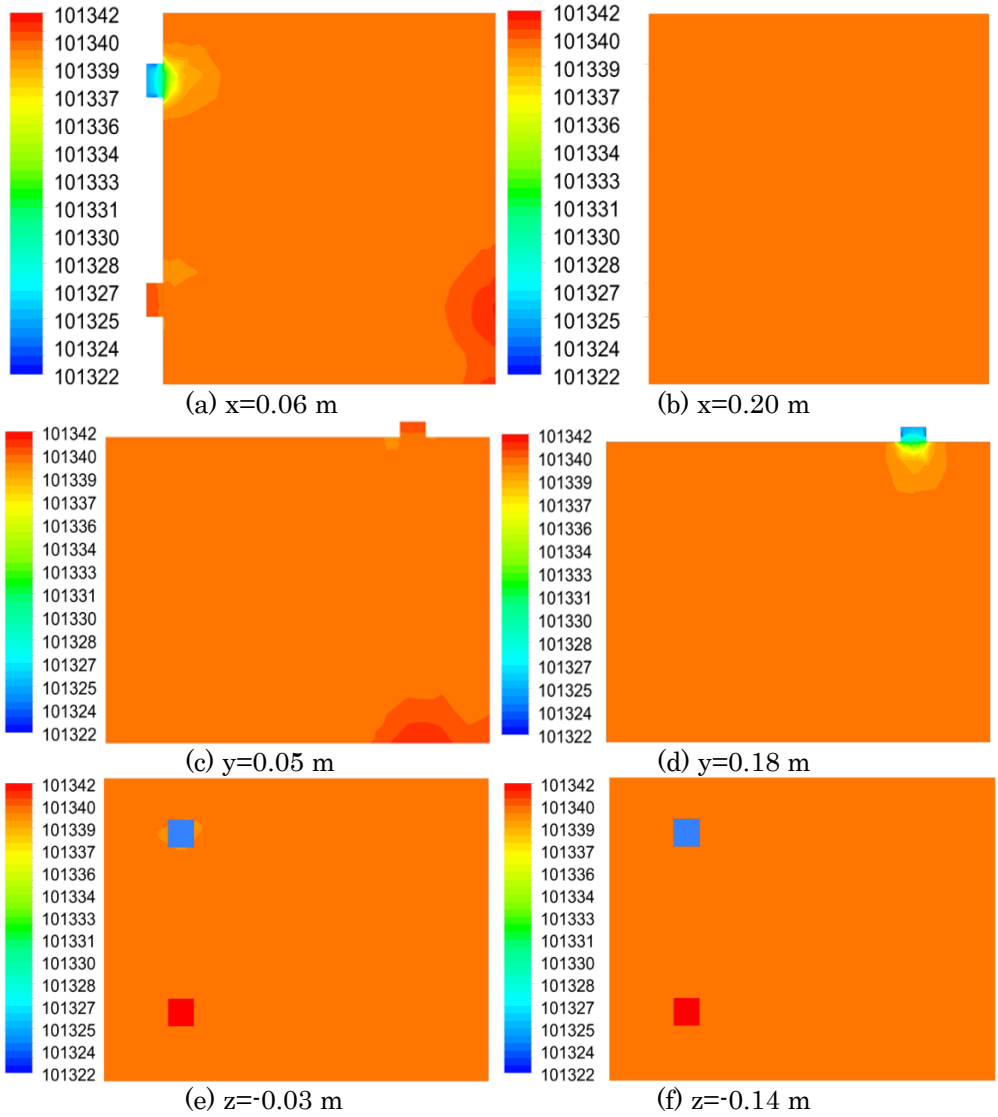

Fig 8: Distribution of the total pressure.

Turbulent Kinetic Energy

Fig 9 shows the distribution of turbulent kinetic energy in the different considered planes defined by x= 0.06 m, x= 0.20 m, y= 0.05 m, y= 0.18 m, z= -0.03 m and z= -0.14 m. According to these results, it has been noted that the turbulent kinetic energy presents low values at the whole inlet of the box prototype. From this hole, a slightly increase of the turbulent kinetic energy has been observed in the discharge area, created in the bottom of the box prototype and near the opposite wall. In this area, a wake zone characteristic of the maximum values of the turbulent kinetic energy appears. This fact can be explained by the recirculation zone created in the whole area of the box prototype. Far from of this domain, the turbulent kinetic energy decreases and reaches a very weak value in the top of the box prototype. However, in the hole outlet, a second wake zone appears, with a maximum value of the turbulent kinetic energy equal to k= 0.398 $m^2.s^{-2}$.

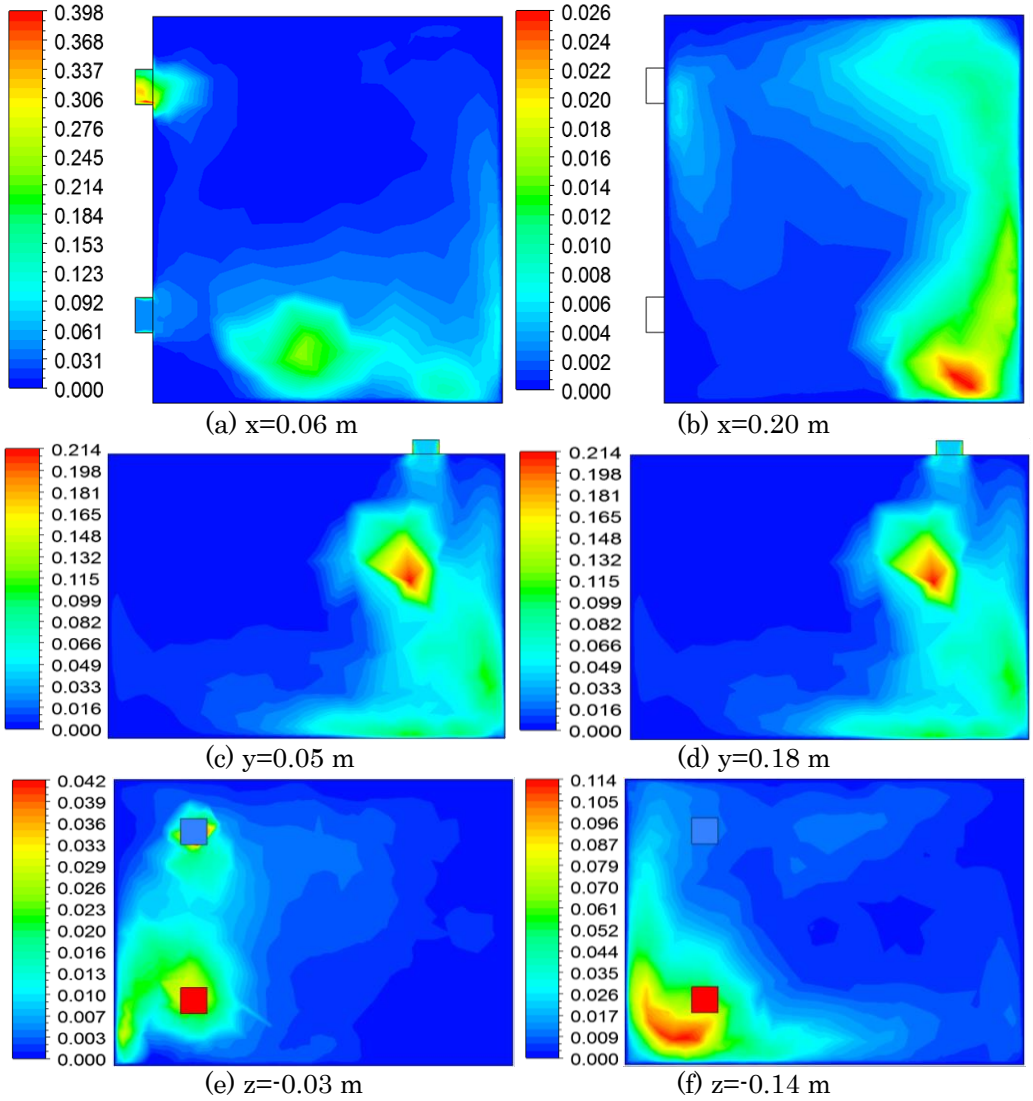

Fig 9: Distribution of the turbulent kinetic energy

Turbulent Viscosity

Fig 10 shows the distribution of the turbulent viscosity in the different considered planes defined by x= 0.06 m, x= 0.20 m, y= 0.05 m, y= 0.18 m, z= -0.03 m and z= -0.14 m. According to these results, it has been noted that the turbulent viscosity presents low values at the whole inlet of the box prototype. From this hole, a slightly increase of the turbulent viscosity has been observed in the discharge area, created in the bottom of the box prototype and near the opposite wall. In this area, a wake zone characteristic of the maximum values of the turbulent viscosity appears. This fact can be explained by the recirculation zone created in the whole area of the box prototype. Far from of this domain, the turbulent viscosity decreases and reaches a very weak value in the top of the box prototype. However, in the hole outlet, a second wake zone appears, with a maximum value of the turbulent viscosity equal to μ_t= 0.00196 $kg.m^{-1}.s^{-1}$.

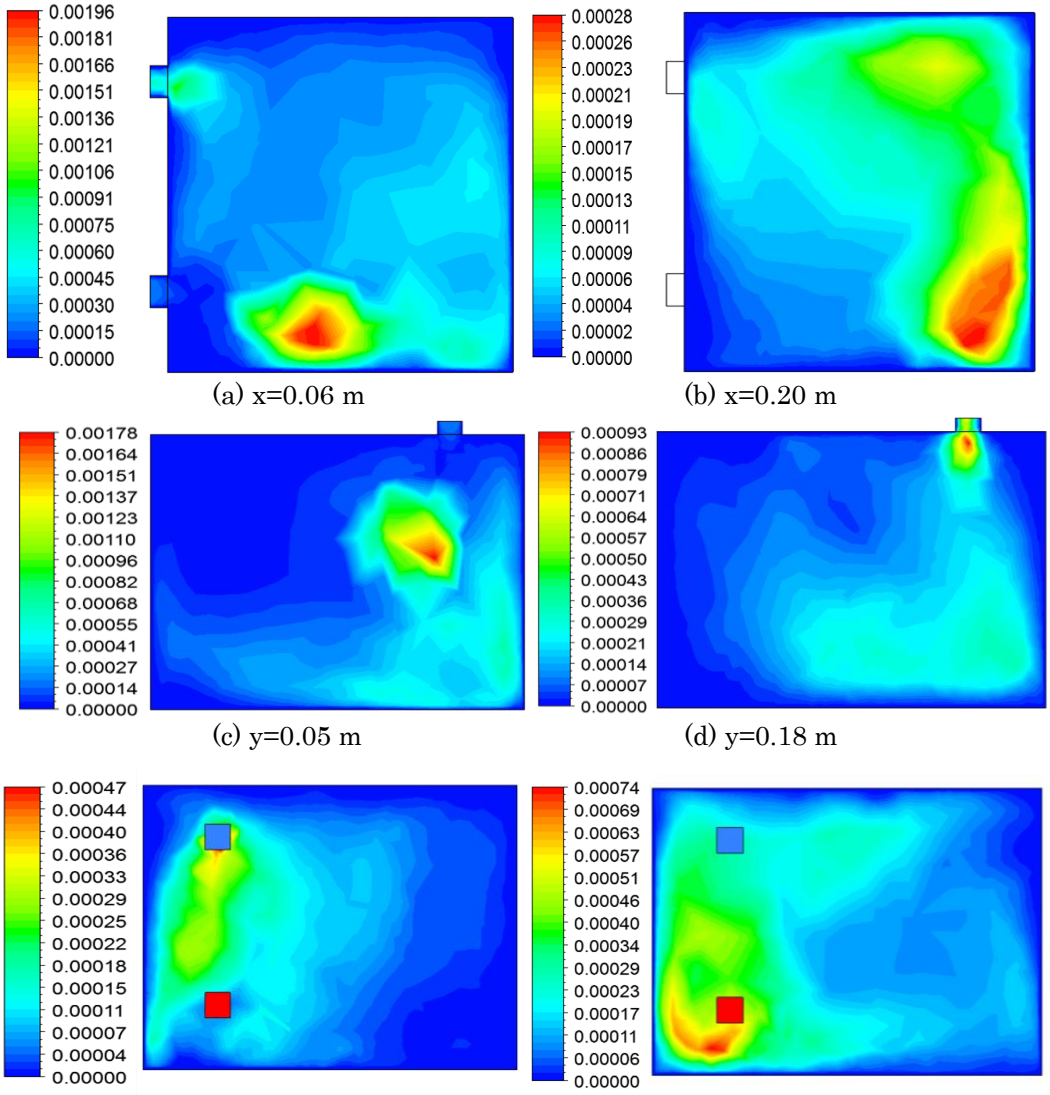

Fig 10: Distribution of the turbulent viscosity

Conclusion

In this work, we are interested in the study of the heat ventilation of a box prototype with a k-ω turbulence model. In this prototype, a solar system is integrated to supply the whole inlet with a hot air. From this hole, a discharge area has been generated until the opposite wall where the direction of the velocity is modified in two directions. The first ascending flow generates the recirculation zone appeared in the whole area of the box prototype. The second descending flow generates the dead zone appeared in the down area. Through the whole outlet, the exiting movement of the air flow appears with a maximum value. To accurate the numerical results, the meshing effect on the numerical results was studied to choose the optimal mesh with a minimum calculated time. The numerical results were compared using anterior results developed in our laboratory. The good agreements confirm the validity of the numerical method. In the future, we propose to study the size of the air distribution system on the aerodynamic characteristics in the considered box prototype. The use of the adequate system is the key to reduce the energy consumption and to guess a continuous heating with zero energy.

Acknowledgements

The authors would like to thank the Laboratory of Electro Mechanic Systems (LASEM) members for the financial assistance.

Nomenclature

E: Total energy (J)
F_i: Force components on the i direction (N)
G_k: Generation of the turbulent kinetic energy ($kg.m^{-1}.s^{-3}$)

G_b: Generation of turbulence kinetic energy ($kg.m^{-1}.s^{-3}$)
G_v: Production of turbulent viscosity ($kg.m.s^{-2}$)
$G\omega$: Generation of the dissipation rate of the turbulent kinetic energy ($kg.m-1.s^{-3}$)
H: Height (m)
h: Thermal enthalpy ($J.kg^{-1}$)
k: Turbulent kinetic energy ($m^2.s^{-2}$)
l: Length (m)
p: Pressure (Pa)
P_r: Prandt number
Q_H: Heat source or sink per unit volume ($kg.m^{-1}.s^{-3}$)
q_i: Diffusive heat flux (J)
Re: Reynolds number (dimensionless)
R_k: Constant of the k-ω turbulence model (dimensionless)
R_ω: Constant of the k-ω turbulence model (dimensionless)
S: Scalar measure of the deformation tensor
S_i: Mass-distributed ($kg.m^{-2}.s^{-2}$)
S_{ij}: Mean rate-of-strain tensor (s^{-1})
S_ω: Source terms of the specific dissipation rate of the turbulent kinetic energy ($kg.m-1.s^{-3}$)
S_k: Source terms of the turbulent kinetic energy ($kg.m^{-1}.s^{-3}$)
T: Temperature (K)
t: Time (s)
u: Velocity components ($m.s^{-1}$)
u_i': Fluctuating velocity ($m.s^{-1}$)
x_i: Cartesian coordinate (m)
x: Cartesian coordinate (m)
y: Cartesian coordinate (m)
Y_M : Fluctuating dilatation in compressible turbulence ($kg.m^{-1}.s^{-3}$)
Y_k : Turbulence dissipation of k ($kg.m^{-1}.s^{-3}$)
Y_ω : Turbulence dissipation of ω ($kg.m^{-1}.s^{-3}$)
z: Cartesian coordinate (m)
U: Free-stream velocity ($m.\ s^{-1}$)
α_0 : Constant of the k-ω turbulence model (dimensionless)
α_∞ : Constant of the k-ω turbulence model (dimensionless)
α^*_∞: Constant of the k-ω turbulence model (dimensionless)
δ_{ij}: Kronecker delta function (dimensionless)
μ: Dynamic viscosity (Pa.s)
μ_t: Turbulent viscosity (Pa.s)
μ_{eff}: Effective viscosity (Pa.s)
ω:: Specific dissipation rate (s^{-1})
ρ: Density ($kg.m^{-3}$)
β_I : Constant of the k-ω turbulence model (dimensionless)
σ_k : Turbulent Prandtl number for k (dimensionless)
σ_ω : Turbulent Prandtl number for ω (dimensionless)
τ_{ij} : Viscous shear stress tensor (Pa)
$(\tau_{ij})_{eff}$: Deviatoric stress tensor (Pa)
Φ: Equivalence ratio (dimensionless)
Γ_k: Effective diffusivity of k (Pa.s)
Γ_ω: Effective diffusivity of ω (Pa.s)
Ω : Swirl number (dimensionless)
Ω_{ij}: Rate of rotation tensor (s^{-1})

References

Ahmed A.Q., GAO S.A., Kareem A.K., 2016. A numerical study on the effects of exhaust locations on energy consumption and thermal environment in an office room served by displacement ventilation. Energy Conversion and Management, 117, 74-85.

Awbi H.B., 1998. Calculation of convective heat transfer coefficients of room surfaces for natural convection. J. Energy and Building, 28, 219-227.

Bu Z., Shinsuke K., W 2011. Ind-induced ventilation performances and airflow characteristics in an areaway-attached basement with a single-sided opening, Building and environment, 46, 911-921.

Caciolo M., Stabat P., Marchio D., 2011. Full scale experimental study of single-sided ventilation: Analysis of stack and wind effects. J. Energy and Building, 43, 1765-1773.

Chan A.L.S., 2015. Investigation on the appropriate floor level of residential building for installing balcony, from a view point of energy and environmental performance. A case study in subtropical Hong Kong. J. Energy, 85, 620-634.

Driss S., Driss Z., Kammoun I., 2016. Computational study and experimental validation of the heat ventilation in a living room with a solar patio system. J. Energy and building, 119, 28-40.

Driss S., Driss Z., Kammoun I., 2015. Numerical simulation and wind tunnel experiments on wind-induced natural ventilation in isolated building with patio. J. Energy, 90, 917-925.

Driss Z., Mlayah O., Driss S., Driss D., Maaloul M., Abid M.S., 2015. Study of the bucket design effect on the turbulent flow around unconventional Savonius wind rotors. J. Energy, 89, 708-729.

Driss Z., Mlayeh O., Driss D., Maaloul M., Abid M.S., 2014. Numerical simulation and experimental validation of the turbulent flow around a small incurved Savonius wind rotor. J. Energy, 74, 506-517.

Driss Z., Mlayah O., Driss S., Maaloul M., Abid M.S., 2016. Study of the incidence angle effect on the aerodynamic structure characteristics of an incurved Savonius wind rotor placed in a wind tunnel. J. Energy, 113, 894-908.

Gilani S., Montazeri H., Blocken B., 2016. CFD simulation of stratified indoor environment in displacement ventilation: Validation and sensitivity analysis. J. Building and Environment, 95, 299-313.

Lo J., Novoselac A., 2013. Effect of indoor buoyancy flow on wind-driven cross ventilation. J. Building Simulation, 6, 69-79.

Lo L.J., Novoselac A., 2012. Cross ventilation with small openings: Measurements in a multi-zone

test building, Building and Environment, 57, 377–386.

Mao N., Song M.J., Chan M.Y., Pan D.M., Deng S.M., 2016. Computational fluid dynamics (CFD) modelling of air flow field, mean age of air and CO2 distributions inside a bedroom with different heights of conditioned air supply outlet. J. Applied Energy, 164, 906-915.

Martins N.R., Graça G.C. Da., 2016. Validation of numerical simulation tools for wind-driven natural ventilation design, J. Building Simulation, 9, 75-87.

Nada S.A., El-Batsh H.M., Elattar H.F., Ali N.M., 2016. CFD investigation of airflow pattern, temperature distribution and thermal comfort of UFAD system for theater buildings applications. J. Building Engineering, 6, 274-300.

Nielsen P.V., Liu L., Peng L., Li Y., 2016. The Status of Computational Fluid Dynamics. In: 12th REHVA World Congress Clima 2016, Aalborg, Denmark.

Niu J., 2004. Some significant environmental issues in high-rise residential building design in urban areas. J. Energy and Building, 36, 1259-1263.

Premrov M., Leskovar V.Z., Mihalic K., 2016. Influence of the building shape on the energy performance of timber-glass buildings in different climatic conditions. J. Energy, 108, 201-211.

Park J., Sun X., Choi J., Rhee G.H., 2017. Effect of wind and buoyancy interaction on single-sided ventilation in a building. J. of Wind Engineering & Industrial Aerodynamics, 171, 380–389.

Pasut W., De Carli M., 2012. Evaluation of various CFD modeling strategies in predicting airflow and temperature in a naturally ventilated double skin façade. J. Applied Thermal Engineering, 37, 267–274.

Rauf A., Crawford R.H., 2015. Building service life and its effect on the life cycle embodied energy of buildings. J. Energy, 79, 140–148.

Sedki A., Hamza N., Zaffagnini T., 2013. Effect of Orientation on Indoor Thermal Neutrality in Winter Season in Hot Arid Climates Case Study: Residential Building in Greater Cairo. I.J. of Engineering and Technology (IACSIT), 6, 712-716.

Varughese J.P., John M.M., 2016. Effect of emissivity of shading device and air flow inside cavity of Double Skin Facade for energy saving and Thermal Comfort in buildings: A CFD modeling. I. Conference on Energy Effcient Technologies for Sustainability, pp. 815–820.

Wang L., Wong N.H., 2009. Coupled simulations for naturally ventilated rooms between building simulation (BS) and computational fluid dynamics (CFD) for better prediction of indoor thermal environment. J. Building and Environment, 44, 95–112.

Yang W., Wong N.H., Li C.Q., 2016. Effect of Street Design on Outdoor Thermal Comfort in an Urban Street in Singapore. J. of Urban Planning and Development, 142, 11-19.

Zhou C., Wang Z., Chen Q., Jiang Y., Pei J., 2014. Design optimization and field demonstration of natural ventilation for high-rise residential buildings. J. Energy and Building, 82, 457–465.

Zhang Z., Zhang W., Zhai Z.J., Chen Q.Y., 2007. Evaluation of various turbulence models in predicting airflow and turbulence in enclosed environments by CFD: Part 2 Comparison with experimental data from literature. HVAC & R Research, 13, 871-886.